



Structure and surface properties of ceria-modified Ni-based catalysts for hydrogen production



S. Damyanova^{a,*}, B. Pawelec^b, R. Palcheva^a, Y. Karakirova^a, M.C. Capel Sanchez^b, G. Tyuliev^a, E. Gaigneaux^c, J.L.G. Fierro^b

^a Institute of Catalysis, Bulgarian Academy of Sciences, 1113 Sofia, Bulgaria

^b Instituto de Catálisis y Petroleoquímica, CSIC, Cantoblanco, 28049 Madrid, Spain

^c Université catholique de Louvain, Institute of Matter Condensed and Nanosciences, Molecules, Solids and Reactivity, Croix du Sud, B-1348 Louvain la Neuve, Belgium

ARTICLE INFO

Keywords:

Ni catalysts

Mixed CeO₂-Al₂O₃ oxides

Dry methane reforming

Hydrogen

Characterization

ABSTRACT

Series of Ni catalysts supported on alumina and mixed xCeO₂-Al₂O₃ oxides with different CeO₂ content (1–12 wt %) were prepared by impregnation method. The effect of CeO₂ loading on the structure and catalytic properties of supported Ni catalysts in dry methane reforming was studied. The texture, structure and surface properties of the catalysts in their calcined, reduced and used state were studied by using different techniques such as: adsorption-desorption isotherms, XRD, UV-vis DRS, XPS, Raman, H₂-TPR, EPR, TPO and TEM. Variation in the electronic environments of the cerium and nickel as a function of the CeO₂ content and pretreatment was observed for CeO₂-containing Ni catalysts. The couples Ni²⁺/Ni⁰ and Ce³⁺/Ce⁴⁺ were detected in the oxidic, reduced and spent ceria-loaded Ni catalysts. CeO₂-containing Ni catalysts exhibited higher activity and stability with time on stream relative to that of alumina-supported Ni. The obvious difference in the behaviors of Ni/xCeO₂-Al₂O₃ and Ni/Al₂O₃ was related to the difference in their dispersions. Small nanoparticles of 4.7–6.3 nm were observed for CeO₂-modified catalysts assuring their high activity and resistance to carbon deposition. The highest activity and stability of Ni catalyst with 6 wt.% CeO₂ was due to the higher electron density and accessibility of the active sites caused by the close contact between nickel and cerium species. While, Ni/Al₂O₃ catalyst exhibited low activity and carbon resistant due to the agglomeration of nickel particles up to 20 nm.

1. Introduction

Hydrogen was considered to be an ideal energy carrier to support sustainable energy development due to the increasing of the shortage of fossil fuels and environmental problems. One of the main renewable resources for hydrogen production is the biomass. The fermentation of biomass can be oriented to formation of bioethanol or biogas [1], which contains two greenhouses gases: CH₄ and CO₂. Among the several reforming processes, reforming of methane with CO₂ (dry or biogas reforming) to hydrogen or hydrogen-rich synthesis gas has increasing attention. Dry methane reforming (DMR) process yields a synthesis gas with molar H₂/CO ratio of about one that is suitable for Fisher-Tropsch synthesis [2]. A serious problem of this process was the fast catalyst deactivation caused by the coke deposition [3,4]. Thermodynamics analysis indicated that the carbon deposition in DMR is inevitable within the temperature range from 573 K to 1273 K [5]. Different approaches have been proposed in the search of improving the catalyst performance and stability in this reaction that are mainly focused on: (i)

the improvement of resistance towards coke formation; (ii) the development of suitable support to enhance the catalyst efficiency; (iii) the relation between the characteristics and activity of supported metal species and (iv) the reaction mechanism [6].

Various supported noble metals, such as Pt, Pd, Ir and others [5] in DMR exhibited increasing catalyst resistance to coke deposition and high activity and selectivity depending on the support kind. However, due to their high cost and limited availability, nickel based catalysts have been widely investigated and employed as alternatives to noble metals in reforming processes, especially for steam methane reforming, due to their advantages: low cost and wide availability [6–8]. However, Ni catalysts supported on alumina deactivate quickly under reaction conditions as a consequence of carbon deposition, caused by the agglomeration of nickel particles. Therefore, the development of Ni-based catalysts for reforming processes with a high resistance to coke formation is still a challenge.

There are different ways to make Ni catalysts resistant to coke deactivation that involve different synthesis methods such as from

* Corresponding author.

E-mail address: soniad@ic.bas.bg (S. Damyanova).

hydrotalcite precursors to obtain the so called “intelligent” reforming catalysts [9–12], by adding of promoters, like traces of noble metals [12,13] or by selection of suitable support [14–16]. Controlling the size of nickel ensembles by adding cobalt or copper [17–19] to bimetallic Ni-based catalysts or controlling the metal-support interaction by introducing metal nanoparticles into the framework of the oxide support [21] led to obtain catalyst with increased resistance to deactivation.

The acidity and basicity of the support has a significant influence on the metal-support interaction, as well as on the adsorption and reactions of methane and carbon dioxide. For example, the supports with basic properties, such as La_2O_3 or MgO , or adding basic promoters onto the catalyst surface, offers an increase of CO_2 adsorption resulting in an increase of adsorbed oxygen atoms (O_{ad}) [6,10]. The pioneering investigation of Verykios and co-workers about understanding the role of La_2O_3 as support for carbon elimination in DMR [22,23] concluded that the carbon dioxide is adsorbed and reacted with La_2O_3 support to form carbonates, like $\text{La}_2\text{O}_3\text{CO}_3$, which react with the carbon species from methane decomposition to form carbon monoxide.

It is well known that the ceria or ceria-containing materials among different supports are ones of the most promising materials in suppression of catalyst deactivation by coke deposition due to the unique properties of CeO_2 [20]: high reducibility, oxygen mobility and oxygen storage capacity (OSC) caused by the presence of the redox couple $\text{Ce}^{4+} \leftrightarrow \text{Ce}^{3+}$ [24]. However, the positive effect of ceria on carbon removal significantly depends on the CeO_2 concentration and on the method of catalyst preparation, which can affect the metal-support interaction, as well as the dispersion of the active metal sites. It was shown that addition of zirconia to ceria improves the OSC due to the formation of ceria-zirconia solid solution, which favors the mechanism of carbon removal from metallic particle over $\text{Ni}/\text{Ce}_x\text{Zr}_{1-x}\text{O}_2/\text{Al}_2\text{O}_3$ catalysts [15]. Mixed oxides, like $\text{CeO}_2\text{-ZrO}_2$ and $\text{CeO}_2\text{-Al}_2\text{O}_3$ prepared by using surfactant, exhibited a high activity and stability in DMR due to the enhanced Ni reducibility [25]. The formation of graphitic deposits on Ni catalysts prepared by citric acid method was limited by the presence of CeAlO_3 species and the small Ni crystallite sizes formed during the catalyst activation [26]. $\text{Ni}/\text{Ce}/\text{Al}$ catalysts prepared as aerogel showed higher activity and stability than that prepared as xerogel due to the higher specific surface area, porosity and homogeneity of Ni species [27]. The amount of carbonaceous deposits for Ni catalyst supported over binary $\text{CeO}_2\text{-ZrO}_2$ or $\text{CeO}_2\text{-TiO}_2$ systems prepared by coprecipitation was depending on the CeO_2 content. [28,29]. An optimum CeO_2 loading was responsible for the improved activity of these catalysts in DMR related to the higher surface density of the active sites and redox properties of CeO_2 .

Using the incipient wetness-impregnation method as preferred method for synthesis of supported catalysts on carriers with a high surface area due to its economical and facile approach, noble based catalysts supported on alumina and zirconia modified with ceria have been successfully obtained for DMR in previously our works [30–32]. However, it is usually accepted that this method is less effective for the synthesis of Ni based catalysts due to the difficulty to obtain highly dispersed metal Ni nanoparticles that are resistance to deactivation, which have the tendency to minimize the surface energy by increasing the interactions with the support to prevent the agglomeration.

In the present work we attempted to stabilize well dispersed Ni particles by combining the high surface area of $\gamma\text{-Al}_2\text{O}_3$ with the unique properties of ceria, using the conventional synthesis approach. The role of the metal-support interaction and metal particle size, determining the activity and stability of Ni based catalysts for DMR as a function of CeO_2 content (1, 3, 6 and 12 wt.%) was evaluated. Thus, the subject of the present work was to investigate the effect of CeO_2 content on the structure and surface properties of $x\text{CeO}_2\text{-Al}_2\text{O}_3$ -supported Ni catalysts in order to achieve an optimally designed catalyst, exhibiting a maximal efficiency for DMR. The obtained samples were characterized by using a combination of N_2 adsorption-desorption isotherms, X-ray diffraction (XRD), diffuse reflectance spectroscopy (UV-vis DRS), X-ray

photoelectron spectra (XPS), Raman spectroscopy, temperature programmed reduction (TPR), thermogravimetric analysis (TGA), temperature programmed oxidation (TPO), electron paramagnetic resonance (EPR) and transmission electron microscopy (TEM).

2. Experimental

2.1. Sample preparation

Mixed $x\text{CeO}_2\text{-Al}_2\text{O}_3$ oxides were obtained by impregnation of γ -alumina support of $S_{\text{BET}} = 248 \text{ m}^2/\text{g}$ with an aqueous solution of $(\text{NH}_4)_3[\text{Ce}(\text{NO}_3)_6]$ with appropriate CeO_2 concentration ($x = 1, 3, 6$ and 12 wt%). Before impregnation, $\gamma\text{-Al}_2\text{O}_3$ carrier was calcined at 650 °C for 4 h. The solids were dried and calcined in air at 110° and 600 °C for 12 and 2 h, respectively. Supported Ni catalysts were synthesized by wetness impregnation of $x\text{CeO}_2\text{-Al}_2\text{O}_3$ oxides with aqueous precursor solution of $\text{Ni}(\text{NO}_3)_2\text{xH}_2\text{O}$ followed by drying and calcination in air at 100 °C and 550 °C for 12 and 2 h, respectively. The theoretical Ni content was 10 wt.%. The samples were denoted as $\text{Ni}/x\text{CeO}_2\text{-Al}$, where x is the CeO_2 content.

2.2. Methods

Specific surface area (S_{BET}), total pore volume (V_p) and average pore size diameter (D_p) of the samples were determined by N_2 adsorption-desorption isotherms recorded at 77 K with a Micromeritics TriStar 3000 apparatus. The samples were previously out-gassed under vacuum at 150 °C for 24 h. The surface area was calculated according to the BET method.

XRD analysis was performed according to the step scanning procedure (step size 0.02° and 0.5 s) with a computerized Seifert 3000 diffractometer, using Ni-filtered $\text{Cu K}\alpha$ radiation ($\lambda = 0.15406 \text{ nm}$) and PW 2200 Bragg-Brentano $\theta/2\theta$ goniometer equipped with a bent graphite monochromatic and an automatic slit. The assignment of the various crystalline phases was based on the JPDs powder diffraction file cards. The average particles size (D_{XRD}) of CeO_2 was calculated by Scherer equation.

UV-vis DRS spectra of the samples were recorded by Varian Cary 5000 UV-vis spectrometer equipped with an integration sphere. The spectra were taken at room temperature in the range of 200–800 nm for the samples diluted in KBr.

XPS of calcined, reduced and spent catalysts were obtained with a Surface Science Instruments SSX-100 model 206 spectrometer equipped with a monochromatized micro focused Al X-ray source, operating at 10 kV and 12 mA. The residual pressure inside the analysis chamber was about 10^{-6} Torr. The flood gun energy was adjusted at 8 eV with a fine-meshed nickel grid placed 3 mm above the sample surface. The pass energy was 150 eV and the spot size were 1000 μm , leading to an energy resolution of 1.6 eV. The binding energy (BE) scale of the spectrometer was calibrated with respect to the $\text{Au } 4f_{7/2}$ peak of gold fixed at 83.98 eV and the BEs of O 1s, Al 2p, Ni 2p and Ce 3d electrons were referenced to the C 1s band at 284.8 eV. The peak decomposition was performed using the Casa XPS program (Casa Software, UK), assuming a 85/15 Gaussian/Lorentzian product function. In order to obtain the XPS atomic ratio between $\text{Ni } 2p_{3/2}$, Ce 3d and Al 2p the normalized intensities of $\text{Ni } 2p_{3/2}$, Ce 3d and Al 2p were calculated by multiplying the relative area of the corresponding peaks by the sensitivity factors. The reduction of the samples was performed ex-situ under H_2/He flow (60 cm^3/min) at 550 °C for 1.5 h. After reduction, the reactor was cooled down to room temperature under 10% H_2/He and transported to XPS apparatus under isoctane.

TPR experiments were conducted on Micromeritics 2900 equipment provided with a TCD and interfaced to a data station. TPR profiles were recorded on the previously degassed sample (in He at 473 K for 0.5 h, $m = 0.05 \text{ g}$) by passing of 10% vol. H_2 in Ar up to a final temperature of 1000 °C with a total flow rate of 50 ml/min and heating rate of 15 K/

min. A cold trap was placed before the thermo-conductivity detector (TCD) to remove water from the exit stream.

EPR spectra of calcined, reduced and spent Ni catalysts were recorded as a first derivative of the absorption signal of a JEOL JES-FA 100 EPR spectrometer. The spectrometer operating in X-band equipped with a standard TE₀₁₁ cylindrical resonator. The samples were placed in a special quartz reactor and were fixed in the cavity center. The Varied Temperature Controller ES-DVT4 was used to permit detection of EPR spectra at temperatures from 123 to 298 K. Desired temperature can be easily obtained by sending liquid nitrogen at a temperature, which is controlled by the EPR spectrometer data system computer to the sample area.

The amount of deposited carbon on the catalyst surface during the reaction was determined by TGA/SDTA851 equipment (Mettler Toledo) by measuring the weight change during the temperature-programmed oxidation (TPO) of spent catalysts. TPO tests have been carried out in a 20% O₂/N₂ mixture by raising the temperature from room temperature to 900 °C at a rate of 10 °C/min. Prior to the TPO experiments, the sample (ca. 30 mg) was pretreated at 500 °C for 1 h in N₂ flow (10 °C/min; 200 ml/min flow rate) in order to homogenize coke and to remove the volatile compounds. One the sample was cooled to 30 °C (5 °C/min), a burning of coke was carried out in a 20% O₂/N₂ mixture by raising the temperature from room temperature to 900 °C at a rate of 10 °C/min. The amount of coke and the reactant/products mixture located in the pores of catalyst was calculated by the difference between initial and final weight of the sample, with the initial weight taken as the mass of the sample after pretreatment with N₂ at 500 °C for 1 h.

Raman spectra were recorded in a commercial micro-Raman system (Dilor Labram Model) equipped with a 20 mW He-Ne laser emitting at 632.8 nm and a holographic notch filter from Kaiser Optical Systems, Inc. (model Super Notch-Plus). All Raman spectra were recorded at room temperature.

TEM images of reduced and spent catalysts were recorded on a JEOL JEM-3010 transmission electron microscope (300 kV, 1.7 Å point resolution). The samples were prepared by dropping a suspension containing the catalyst in isopropanol onto amorphous carbon films supported on copper grids. At least ten representative images were taken for each sample. The average particle size was estimated considering the statistical analysis of the particle sizes distribution.

2.3. Test reaction

The reaction of methane reforming with carbon dioxide was carried out in a fixed-bed quartz reactor at atmospheric pressure. Although thermodynamic considerations indicate that the DRM reaction operate at temperatures so high as 700–850 °C, the activity tests were performed at 550 °C to achieve large differences in catalytic activity. Before catalytic test, the sample was crushed and screened to particle diameter of 0.2–0.25 mm before use. The catalyst (0.05 g) was mechanically mixed with calculated amounts of inert, low surface area quartz sand (particle diameter of 0.2–0.25 mm). The catalyst pretreatment by reduction was carried out in situ by heating in a 10% H₂/N₂ flow (50 ml/min) from 350 °C to 550 °C (heating rate 10 K/min) and then reduced at 550 °C for 1.5 h. After that, the sample was purged with flowing nitrogen (60 ml/min) for 40 min to remove the physically adsorbed hydrogen from the surface. The activity test was performed at 550 °C with a reactant gas mixture of CH₄ (20%) and CO₂ (20%) diluted with N₂, as the total flow rate was kept at 100 ml/min. The reaction products were analyzed by gas chromatograph equipped with a 3 m HayeSep D 100/120 (SUPELCO) column and TCD. The conversions of CH₄ and CO₂, as well as the yields of CO and H₂ were calculated by the following equations: X_{CH₄}, % = (C_{CH₄}, in – C_{CH₄}, out)/C_{CH₄}, in x 100, X_{CO₂}, % = (C_{CO₂}, in – C_{CO₂}, out)/C_{CO₂}, in x 100, Yield H₂, % = C_{H₂}, out/2C_{CH₄}, in x 100, Yield CO, % = C_{CO}, out/(C_{CH₄}, in + C_{CO₂}, in) x 100.

Table 1
Textural characteristics and particle size of CeO₂ of calcined Ni/xCeO₂-Al₂O₃ samples.

Sample	S _{BET} (m ² /g)	V _p (cm ³ /g)	D _p (nm)	D _{XRD} CeO ₂ (nm)
Al ₂ O ₃	248	0.92	14.6	–
Ni/Al	187	0.55	11.7	–
Ni/1Ce-Al	193 (228) ^a	0.66 (0.91) ^a	13.2 (15.7) ^a	–
Ni/3Ce-Al	190 (222)	0.70 (0.87)	13.6 (15.7)	5.5 (5.3) ^a
Ni/6Ce-Al	173 (231)	0.65 (0.86)	14.2 (15.7)	6.2 (6.2)
Ni/12Ce-Al	158 (198)	0.48 (0.79)	12.1 (15.4)	9.3 (9.2)

^a Data of supports 4.

3. Results

3.1. Catalysts characterization

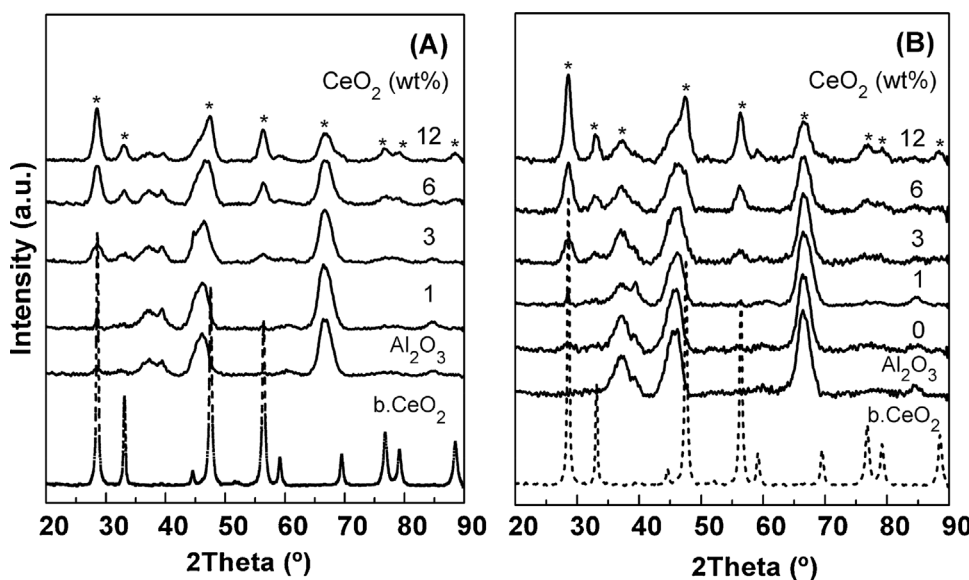
3.1.1. Textural characteristics

The nitrogen adsorption-desorption isotherms of xCeO₂-Al₂O₃ and Ni/xCeO₂-Al₂O₃ samples (not shown) showed curve of IV type with a H1 shaped hysteresis loop, which is typical for mesoporous materials [33]. The textural characteristics S_{BET}, V_p and D_p of the mixed xCeO₂-Al₂O₃ oxides and supported Ni catalysts are listed in Table 1. The stabilization effect of CeO₂ up to 6 wt% on the textural properties of the ceria-modified alumina is clear from the Table 1. The lowest specific surface area is observed for the sample with the highest CeO₂ content (12 wt.%) due to the blockage of alumina pores by cerium oxide species. Addition of nickel to alumina leads to decrease of the S_{BET} of alumina-supported Ni. Ni catalysts supported on ceria-modified alumina exhibit the same tendency in the decrease of the S_{BET} and V_p as a function of CeO₂ content like that observed for supports. (Table 1).

3.1.2. XRD analysis

XRD patterns of calcined xCeO₂-Al₂O₃ oxides and Ni/xCeO₂-Al₂O₃ samples are shown in Fig. 1A and 1B, respectively. For comparison, the XRD of pure alumina and bulk CeO₂ are also included in Fig. 1. The XRD of non-promoted alumina with CeO₂ exhibit peaks at 2θ = 37.2°, 46.2° and 66.4°, corresponding to γ-Al₂O₃ (JCPDS 86–1410). The modification of alumina with different CeO₂ loading leads to a change of the intensity and the shape of XRD peaks of alumina, due to the changes in crystallinity of the samples. Diffraction lines at 2θ = 28.6°, 32.2°, 44.6°, 47.5°, 56.5°, 59.2°, 69.5°, 76.8°, 79.1° and 88.5°, characteristic of CeO₂ phase with fluorite structure (JCPDS 081-0792), are detected in the XRD of CeO₂-containing samples (Fig. 1). The average particle size of CeO₂ in xCeO₂-Al₂O₃ oxides increases with increasing the CeO₂ content (from 5.3 to 9.2 nm for 3CeO₂-Al₂O₃ and 12CeO₂-Al₂O₃, respectively, Table 1), due to the ceria capacity to form aggregates [29]. The intensity of the main line of alumina support at 2θ = 67.1° decreases upon increasing the cerium oxide loading, which is most visible for sample with 12 wt% CeO₂ (Fig. 1A). This could be explained by the existence of some interaction between cerium and aluminium or by the increased coverage of ceria crystallites on alumina. It was shown [35] that the small cerium oxide species at low CeO₂ content (x ≤ 3 wt.%) can interact with alumina support surface to form non-stoichiometric CeO_{2-x}.

The introduction of Ni has not noticeable effect on the particle size of CeO₂ for Ni samples supported on xCeO₂-Al₂O₃ oxides (Table 1). The Ni/Al₂O₃ sample exhibits diffraction features similar to that of alumina at 2θ = 37.1°, 39.3°, 46.1°, 66.5°, 84.7°, however the diffraction peak at 2θ = 37.1° has a higher intensity (Fig. 1B). In addition, a shoulder at about 43° is revealed in the XRD spectra of Ni/xCeO₂-Al₂O₃ samples. These observations should be related to some evidence of NiO formation (2θ = 37.3° and 43.3°, JCPD 78-0643) on the surface of supported Ni samples. On the other hand, the presence of surface nickel aluminate species (at 2θ = 45.8° and 66.4°) could not be excluded. The precise identification of this species is complicated due to the proximity with the lines typical for γ-Al₂O₃ and NiO. However, it could be supposed



that the decreased intensity of the XRD pattern at about 37.1° with the increase of CeO₂ content should be related to the presence of highly dispersed NiO species in some contact with ceria modified support [36,37].

3.1.3. UV-vis DRS

The UV-vis DR spectra of calcined Ni/xCeO₂-Al₂O₃ samples in the wavelengths ranges of 200–800 nm and 550–800 nm are shown in Fig. 2A and 2B, respectively. Non-modified with ceria alumina-supported Ni sample exhibits a strong absorption at 230–350 nm related to the O²⁻→Ni²⁺ charge transfer transition (Fig. 2A). The UV-vis DRS of CeO₂-containing Ni samples show a strong absorption in the range of about 230–490 nm (Fig. 2A). There is a blue shift of the absorption maximum with decrease of the CeO₂ content. It suggests that the intensity of these bands depend on the content and particle size of ceria. This can be explained by the diversity of cation electron environments and the presence of cerium in two oxidation states ascribed to O²⁻→Ce³⁺ and O²⁻→Ce⁴⁺ charge transfers, according to the Refs. [38,39]. This could be caused by the strong interaction of cerium with alumina. The most intensive absorption with a maximum at 300 nm is observed

for the sample with the highest CeO₂ content (Fig. 2A) due to the O²⁻→Ce⁴⁺ charge transfer [40].

The absorption at above 350 nm is associated with the d→d transitions of Ni²⁺ ions. The doublet at 590 nm and 636 nm in the wavelengths range of 550–800 nm (Fig. 2B) suggests the presence of Ni²⁺ ions in tetrahedral coordination, similar to that observed for NiAl₂O₄ [41]. The broad absorption at about 720–780 nm means that Ni²⁺ ions are in octahedral coordination, typical for NiO species. It can be concluded that nickel ions present in different environments.

3.1.4. XPS analysis

The oxidation state of metal components and surface composition of calcined, reduced and spent supported Ni catalysts were defined by collecting the XPS of Al 2p, Ni 2p, Ce 3d and C 1s core electron levels. The XPS parameters and surface atomic ratios are listed in Table 2. The BE values of Ni 2p_{3/2} core electrons for calcined un-promoted and CeO₂-promoted samples at 855.8 eV characterize Ni²⁺ ions. It should be noted that this value is slightly higher than that of bulk NiO with BE of about 854.0 eV due to the interaction of nickel species with support [42], but the BE value is lower than that of NiAl₂O₄ spinel with BE of

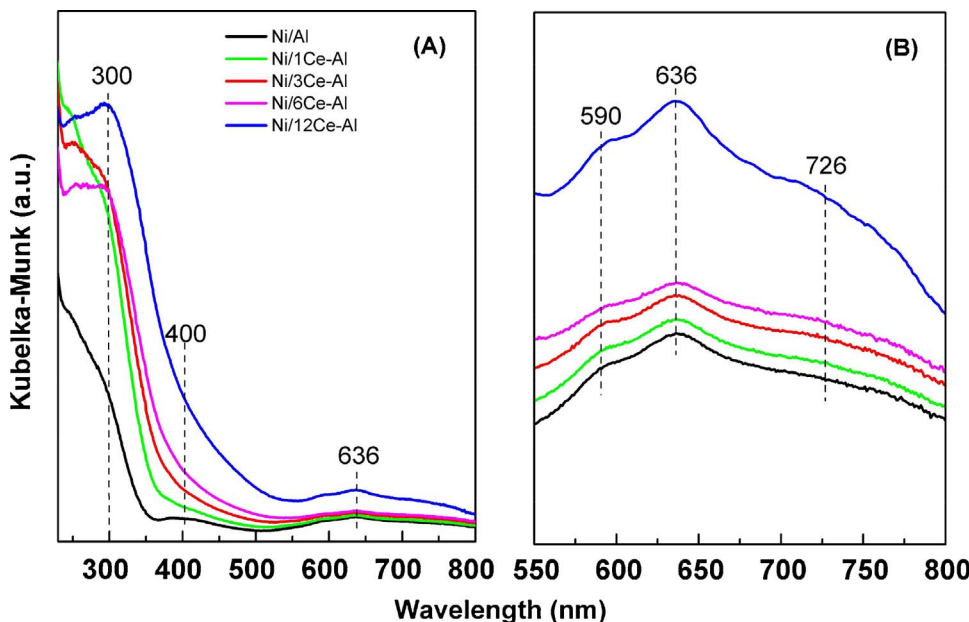


Fig. 2. UV-vis DRS of mixed xCeO₂-Al₂O₃ oxides (A) and Ni/xCeO₂-Al₂O₃ catalysts with different CeO₂ content (B).

Table 2XPS characteristics (BEs, eV, and atomic ratios) of oxidic, reduced and spent Ni/xCeO₂-Al₂O₃ catalysts.

Sample	Ni 2p _{3/2}		Ce3d _{5/2}	Ce ³⁺ /		Ce/Al	Ni/(Al + Ce)	Ni/Ce	C/Al			
	Ni ²⁺	Ni ⁰		(Ce ⁴⁺ + Ce ³⁺)								
<i>Oxidic precursors</i>												
Ni/Al	855.8	–	–	–	–	–	0.063	–	–			
Ni/1Ce-Al	855.8	–	882.1	33 (32) ^a	0.015	0.087	5.96	–	–			
Ni/3Ce-Al	855.8	–	881.9	22 (36)	0.016	0.088	5.38	–	–			
Ni/6Ce-Al	855.8	–	882.1	34 (15)	0.015	0.069	4.58	–	–			
Ni/12Ce-Al	855.8	–	882.3	32 (0)	0.014	0.075	5.46	–	–			
<i>Reduced samples</i>												
Ni/Al	856.1(87) ^b	852.3(13) ^c	–	–	–	0.032	–	–	–			
Ni/1Ce-Al	856.1(86)	852.5 (14)	881.7	35	0.007	0.035	4.95	–	–			
Ni/3Ce-Al	856.1(82)	852.3 (18)	882.3	33	0.009	0.041	4.30	–	–			
Ni/6Ce-Al	855.8 (75)	851.8 (25)	882.4	24	0.009	0.061	5.80	–	–			
Ni/12Ce-Al	856.1(90)	852.4 (10)	882.0	34	0.010	0.056	5.47	–	–			
<i>Spent catalysts</i>												
Ni/Al	856.4 (79) ^b	852.7(21) ^c	–	–	–	0.05	–	0.17	–			
Ni/1Ce-Al	856.4 (77)	852.7 (23)	881.5	36	0.013	0.041	3.85	0.09	–			
Ni/3Ce-Al	856.3 (75)	852.8 (25)	881.4	31	0.014	0.045	4.14	0.07	–			
Ni/6Ce-Al	856.2 (66)	852.7 (34)	881.7	32	0.012	0.053	4.75	0.13	–			
Ni/12Ce-Al	856.3 (82)	852.8 (18)	881.3	40	0.016	0.039	3.88	0.08	–			

^a Support data.^b Ni²⁺ percent. ^c Ni⁰ percent.

about 857 eV [43]. This observation suggests a coexistence of both, the well dispersed NiO and surface species similar to NiAl₂O₄ spinel structure.

The Ce 3d_{5/2} electron level with BE of 882.1 eV is typical for CeO₂ in calcined CeO₂-containing samples (Table 2). Due to the overlapping of the XPS spectra of Ni 2p with Ce 3d core electron levels, the relative concentration of Ce³⁺ for the mixed oxides and supported Ni samples was calculated as a peak area of Ce³⁺ component divided by the total peak area of Ce 3d line. The results in Table 2 suggest a low fraction of Ce³⁺ species on the surface of xCeO₂-Al₂O₃ oxides, as well as on the surface of oxidic Ni catalysts. The fraction of Ce³⁺ for xCeO₂-Al₂O₃ supports decreases with increasing the CeO₂ content, as it is zero in the highest CeO₂-loaded sample, due to the CeO₂ agglomeration.

After deconvolution of the XPS of Ni 2p_{3/2} core electron levels of reduced Ni catalysts two components with BE values at 855.8–856.1 eV and at 851.8–852.4 eV are detected, characterizing the Ni²⁺ and Ni⁰ ions, respectively (Table 2). It is interesting to note, that the BE of Ni 2p_{3/2} electrons of Ni⁰ for reduced Ni catalyst with 6 wt% CeO₂ is shifted to a lower value of 851.8 eV in relation to that of Ni/Al and other CeO₂-containing samples as consequence of the differences in the electron density of the atoms. It means that the nickel atoms on 6CeO₂-Al₂O₃ support acquires a higher electron density. The presence of the both species, Ni²⁺ and Ni⁰ point out that the applied reduction conditions did not lead to complete reduction of the nickel oxide species, probably due to the strong interaction of Ni²⁺ with support, especially in the case of ceria-modified alumina. However, the concentration of Ni⁰ in spent catalysts is increased, suggesting that the reduction of nickel oxide species is going on under the reaction conditions (Table 2). The highest amount of Ni⁰ is detected for spent Ni/6Ce-Al catalyst.

It is not surprising the presence of less metallic Ni⁰ in the sample with 12 wt% CeO₂ considering the close contact at the interface between the Ni clusters and CeO₂ surface, whose extent can increase upon higher temperature reduction [44]. Some covering of Ni sites by cerium species cannot be excluded. The semi-quantitative estimation of the Ce³⁺ ions in the Ni samples clearly indicates that the Ce³⁺/Ce⁴⁺ couple together with the N²⁺/Ni⁰ couple real exist at the nickel-ceria interface of all reduced and spent CeO₂-loaded Ni catalysts.

In relation to alumina-supported nickel catalyst the Ni atoms are well dispersed over the surface of all oxidic CeO₂-loaded samples. It should be noted that all reduced and spent samples reveal XPS atomic Ni/Al + Ce ratios values lower than those of the calcined ones caused

by the sintering of the surface Ni species (Table 2). The values of the XPS Ni/Ce ratios are higher than those of Ni/Al, which means that the nickel atoms are mainly located over cerium species.

The values of the atomic Ce/Al ratios for reduced catalysts decrease with respect to those of the calcined counterparts, due to the sintering of ceria species under hydrogen treatment. However, there is some recovering of the values of Ce/Al ratios for spent catalysts, most probably, caused by some re-dispersion of cerium oxide species under reaction conditions.

It is interesting to note that the Ni catalyst with 6 wt% CeO₂ is characterized with the highest values of the atomic Ni/Al + Ce ratios after reduction and catalytic test (Table 2), irrespective the slightly lower value of this ratio for the spent catalyst. This means that the nickel species have better surface accessibility to the reactant molecules on the modified alumina with 6 wt% CeO₂. Probably, this is caused by the intimate contact between the Ni and Ce atoms, revealed by increasing the BE of Ni 2p_{3/2} from 851.8 to 852.7 eV and by decrease of BE of Ce3d_{5/2} from 882.4 to 881.7 eV for the reduced and spent Ni/6Ce-Al catalyst, respectively, due to a charge transfer [45].

From the change of the atomic C/Al ratios for spent catalysts (Table 2) it is difficult to conclude that there is a linear relation between the amount of carbon deposits and the CeO₂ loading. The highest value of atomic C/Al ratio is detected for non-promoted with ceria Ni catalyst. Within the CeO₂-loaded samples the spent Ni catalyst modified with 6 wt% CeO₂ is characterized with a slightly higher C/Al ratio than those of the other ones. It suggests that the support type, as well as the size of metal particles should have an influence on the carbon deposition.

The surface atomic Ni/Al + Ce ratios values for spent Ni catalysts with 6 and 12 wt% CeO₂ are slightly decreased with respect to those of the H₂-reduced counterparts, most probably caused by the thermal sintering of nickel and ceria species and/or by the partial coverage of nickel by carbon deposits (Table 2). The highest Ce/Al ration detected for spent Ni/12Ce-Al catalyst is accompanied with the lowest Ni/Al + Ce ratio value. This observation should be related to the covering of the Ni active sites with ceria species [44].

3.1.5. TPR

The evaluation of the reducibility and to find the reducible species of the mixed xCeO₂-Al₂O₃ carriers, as well as of the calcined supported Ni catalysts is very important issue in connection with their ability to generate oxygen vacancies. The TPR profiles of the mixed xCeO₂-Al₂O₃

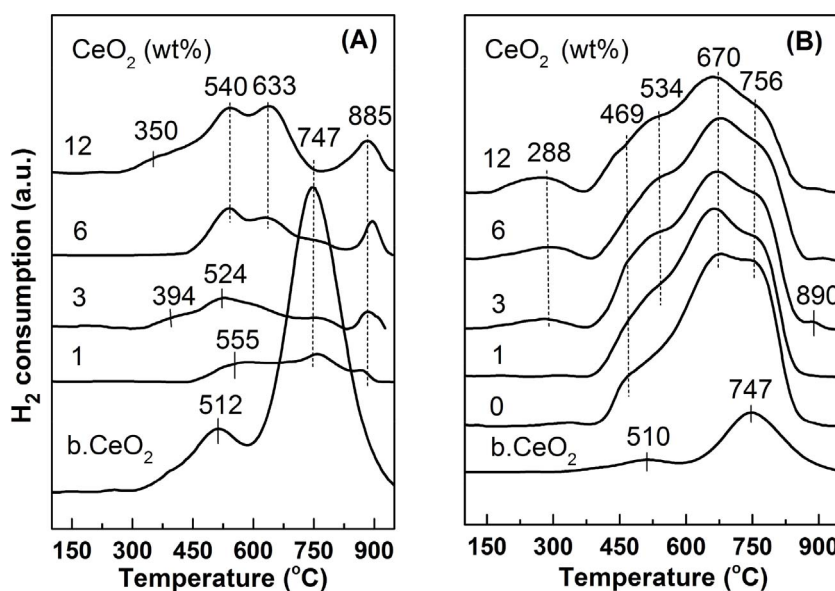


Fig. 3. TPR of calcined mixed $x\text{CeO}_2\text{-Al}_2\text{O}_3$ oxides (A) and supported $\text{Ni}/x\text{CeO}_2\text{-Al}_2\text{O}_3$ catalysts with different CeO_2 content (B).

oxides and $\text{Ni}/x\text{CeO}_2\text{-Al}_2\text{O}_3$ samples with different CeO_2 loading are shown in Fig. 3A and 3B, respectively. The TPR shape of bulk CeO_2 is very similar to that reported in the literature [46] and it can be interpreted as a stepwise reduction process (Fig. 3A). The bulk CeO_2 exhibits two peaks: a small peak at about 508 °C and a large one at 749 °C. The low-temperature peak is due to the reduction of the more easily reducible surface capping oxygen of CeO_2 , followed by generation of oxygen vacancies and surface Ce^{3+} ions, which can be easily oxidized to Ce^{4+} under oxidation conditions [47]. The higher temperature peak is due to the complete reduction of Ce^{4+} to Ce^{3+} by removing of O^{2-} ions of the ceria lattice and formation of Ce_2O_3 .

The addition of ceria to alumina leads to a change of the TPR features of supported ceria. As can be seen in Fig. 3A, the difference in the reductive behaviors of alumina-supported CeO_2 samples of different loadings can be associated with both, the extent and the nature of the interaction between ceria species and alumina. The TPR profiles of $x\text{CeO}_2\text{-Al}_2\text{O}_3$ oxides can be characterized by three temperature regions at 300°–500 °C, 500°–800 °C and at > 800 °C (Fig. 3A). The first region is associated with the reduction of small ceria crystallites and/or surface cerium oxide species in weak interaction with the alumina support surface, whereas the second one is ascribed to the reduction of large CeO_2 crystallites or cerium oxide species and/or cerium atoms in a strong interaction with alumina [48]. The high-temperature peak at 885°–890 °C, which is observed in the TPR of all samples, should be caused by the formation of surface CeAlO_3 associated with the reduction of Ce^{4+} to Ce^{3+} . It has been shown [49] that the reduction of ceria on alumina under hydrogen atmosphere involves at least two reactions: formation of non-stoichiometric cerium oxides (CeO_{2-x}) and surface cerium aluminate (CeAlO_3), depending on the ceria loading. It can be also noted that the increase of peak intensity of CeAlO_3 is accompanied with a decrease of the high-temperature peak intensity due to the reduction of bulk ceria (Fig. 3A).

The TPR profile of non-promoted with ceria $\text{Ni}/\text{Al}_2\text{O}_3$ sample (Fig. 3B) is characterized with a low temperature signal at about 327 °C, due to the reduction of very small NiO particles [50]. The broad hydrogen consumption at higher temperature interval with not well resolved maxima at 469°, 670° and 756 °C should be caused by the reduction of fine complex of nickel oxide species in a more intimate contact with alumina surface. The TPR feature at 756 °C may be related to the reduction of non-stoichiometric surface NiAl_2O_4 species, since a high temperature above 800 °C is required for the reduction of stoichiometric nickel aluminate spinel structure [51,52].

The TPR profiles of $\text{Ni}/x\text{CeO}_2\text{-Al}_2\text{O}_3$ catalysts are different from that

of the non-promoted with ceria Ni sample. The hydrogen consumption increases with the enhancement of CeO_2 content, being seen in Fig. 3B. From the Fig. 3B it can be concluded that the Ni oxide species supported on mixed $\text{CeO}_2\text{-Al}_2\text{O}_3$ oxides show different performance under TPR as a function of the CeO_2 content due to the different extent of interaction between the nickel oxide species and ceria-modified alumina, as well as due to the particle size. It is difficult to define precisely the peaks corresponding to the reduction of cerium or nickel oxide species caused by their overlapping. However, the presence of ceria leads to a change in the relative proportion between the relative peaks intensities at 670° and 756 °C, as the intensity of the higher temperature peak is decreased. It means that the reducibility of nickel oxide species in a strong interaction with alumina surface decreases for CeO_2 -loaded samples, more obviously at CeO_2 content of 12 wt%. A new TPR feature in the lower temperature interval (between 171°–354 °C) is appeared for $\text{CeO}_2\text{-Al}_2\text{O}_3$ -supported Ni samples at CeO_2 content ≥ 3 wt% that can be assigned to the reduction of well dispersed nickel oxide species in some contact with CeO_2 crystallites, as well as to the partial reduction of surface CeO_2 [53,54]. This is explained by the easy reduction of supported fine Ni particles, which in turn facilitate the reduction of cerium oxide species by the hydrogen spillover mechanism. The latter causes the growth of reduction peak at ca. 288 °C with increasing the CeO_2 loading that is accompanied with weakness of the strong interaction between ceria and alumina. This is revealed by the decrease of the band intensity at 890 °C, characteristic of CeAlO_3 formation (Fig. 3B).

3.1.6. EPR

The change of nickel oxidation state in calcined, reduced and spent Ni/Al and $\text{Ni}/x\text{CeO}_2\text{-Al}_2\text{O}_3$ catalysts as a function of CeO_2 content is also detected by EPR. The EPR spectra of the samples are shown in Fig. 4. The EPR parameters for the samples (g factor and line width, ΔH_{pp}) are listed in Table 3. The EPR spectra of calcined Ni/Al and $\text{Ni}/12\text{Ce-Al}$ samples are composed of signal Si1 with g factors of 2.10 and 2.08 and ΔH_{pp} of 61 and 52 mT, respectively (Fig. 4 and Table 3), due to the presence of paramagnetic species of Ni^{2+} ions [55]. Additional EPR lines (signal Si2) with g of 2.29 and 2.28 and with ΔH_{pp} of 132 and 147 are recorded for $\text{Ni}/1\text{Ce-Al}$ and $\text{Ni}/6\text{Ce-Al}$, respectively. This signal can be attributed to the ferromagnetic resonance of metallic nickel [55]. It suggests that ferromagnetic nickel is formed under calcination treatment of the samples up to 550 °C. The most intensive EPR signal Si1 is observed for $\text{Ni}/6\text{Ce-Al}$ sample, which means the presence of more paramagnetic species, containing Ni^{2+} , than in other ones. In addition, a new signal with g = 1.96 is appeared in the EPR spectrum of $\text{Ni}/$

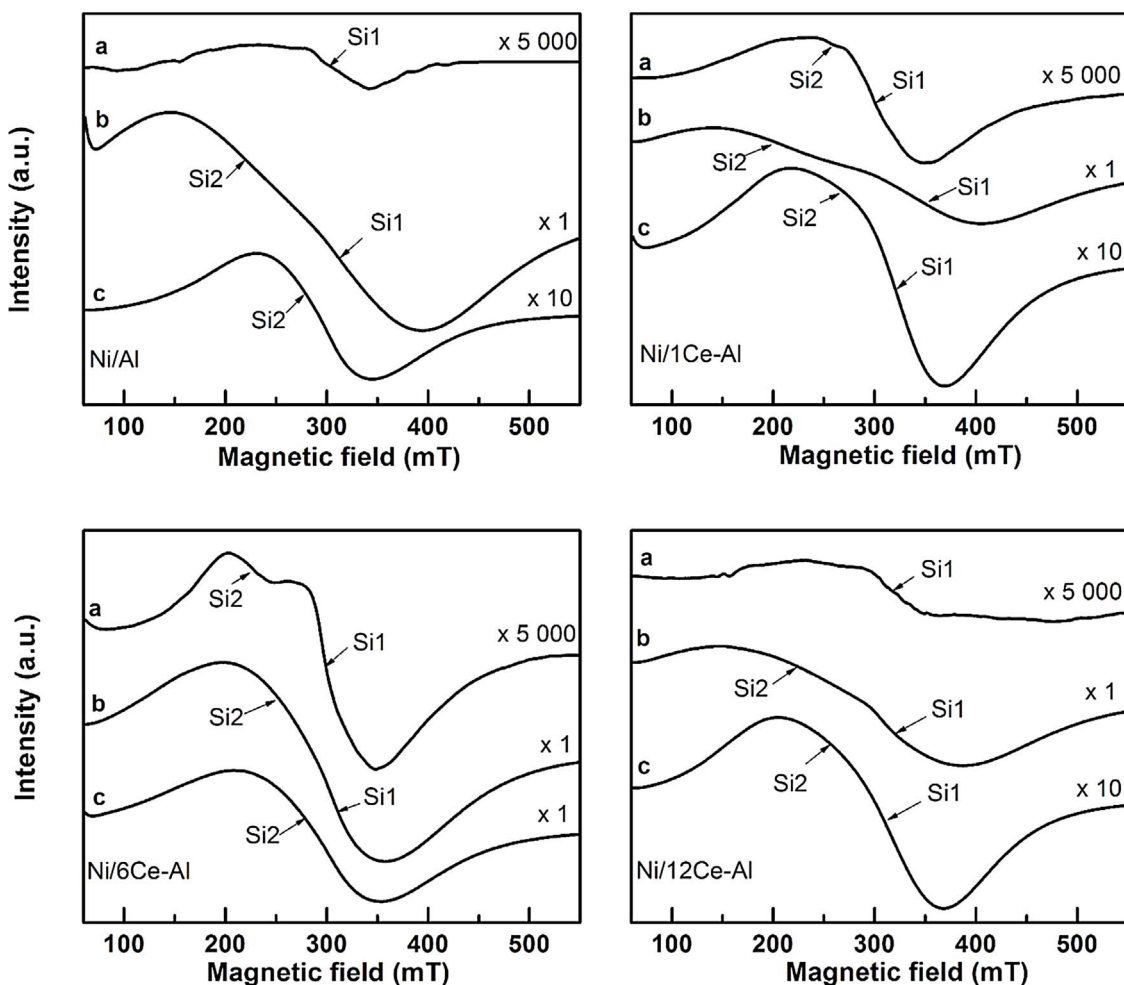


Fig. 4. EPR of calcined (a), reduced (b) and spent (c) $\text{Ni}/\text{xCeO}_2\text{-Al}_2\text{O}_3$ catalysts with different CeO_2 content.

Table 3

EPR characteristics (g -factor and line width) for the $\text{Ni}/\text{xCeO}_2\text{-Al}_2\text{O}_3$ samples at different treatments conditions.

Sample	Conditions	g		ΔH (mT)	
		Si1	Si2	Si1	Si2
Ni/Al	Air	2.10	–	61	–
Ni/Al	H_2 , 550 °C	2.00	2.23	80	240
Ni/Al	$\text{CH}_4 + \text{CO}_2$, 550 °C	–	2.31	–	178
Ni/1Ce-Al	Air	2.22	2.29	74	132
Ni/1Ce-Al	H_2 , 550 °C	2.00	2.27	80	256
Ni/1Ce-Al	$\text{CH}_4 + \text{CO}_2$, 550 °C	2.12	–	152	–
Ni/6Ce-Al	Air	2.20	2.28	58	147
Ni/6Ce-Al	H_2 , 550 °C	2.14	2.33	60	153
Ni/6Ce-Al	$\text{CH}_4 + \text{CO}_2$, 550 °C	–	2.30	–	141
Ni/12Ce-Al	Air	2.08	–	52	–
Ni/12Ce-Al	H_2 , 550 °C	2.15	2.23	60	231
Ni/12Ce-Al	$\text{CH}_4 + \text{CO}_2$, 550 °C	–	2.27	–	162

12Ce-Al. This signal could characterize Ce^{3+} ions in the bulk CeO_2 with fluorite structure with one unpaired electron in the 4f state [56] or the electrons trapped at oxygen vacancies of the ceria lattice [57].

The treatment of the samples under hydrogen atmosphere leads to a change of the shape of the EPR spectra and parameters caused by the reduction of Ni^{2+} species to Ni^0 (Fig. 4). The Si2 signal for all samples is shifted to higher magnetic fields revealed by the higher values of g factor (Table 3). It should be noted that the shape of Si2 is more sensitive to the CeO_2 content than that of signal Si1. The line width of signal Si2 of the samples is broader for reduced Ni/Al (240 mT), Ni/

1Ce-Al (256 mT) and Ni/12Ce-Al (231 mT) owing to sintering of metallic nickel particles [47]. The most intensive EPR signal recorded for Ni/6Ce-Al sample (Fig. 4) means the presence of small clusters of nickel species of Ni^{2+} , as well as of Ni^0 . The high intensity of Si2 for Ni/6Ce-Al sample suggests that Ni^0 species are dominant, which are well dispersed on the catalyst surface demonstrated by the lower value of ΔH_{pp} (153 mT) (Table 3). This correlates with the XPS data (Table 2).

It can be assumed that the different changes in the values of the EPR parameters (g factor and line width) should be explained by the different surroundings of paramagnetic species in the catalysts, depending on the support kind, especially on the CeO_2 content and the treatment conditions.

It was tried to detect the change in the oxidation state of cerium ions in the samples treated at different conditions. The EPR signal corresponding to isolated Ce^{3+} ions didn't detect even at 123 K because the EPR signal of metallic nickel was very intensive and broad. It can be supposed, that there is formation of clusters of Ce^{3+} in close vicinity in a strong dipolar interaction with neighboring Ni^{2+} , but this signal can't be obvious because of similarity with the EPR parameters of ferromagnetic nickel [58].

For all spent catalysts, the intensity and the width of the EPR are decreased, probably caused by the formation of diamagnetic nickel particles, due to their contact with cerium species (Fig. 4). However, the decrease of EPR intensity is lower for Ni/6Ce-Al. On the other hand, there is some overlapping of the Si1 and Si2 signals, which is more evident in the EPR spectra of spent $\text{Ni}/\text{Al}_2\text{O}_3$ and Ni/6Ce-Al catalysts that leads to a change in the EPR parameters due to the change of electronic environment. For Ni/6Ce-Al there is more dipol-dipol

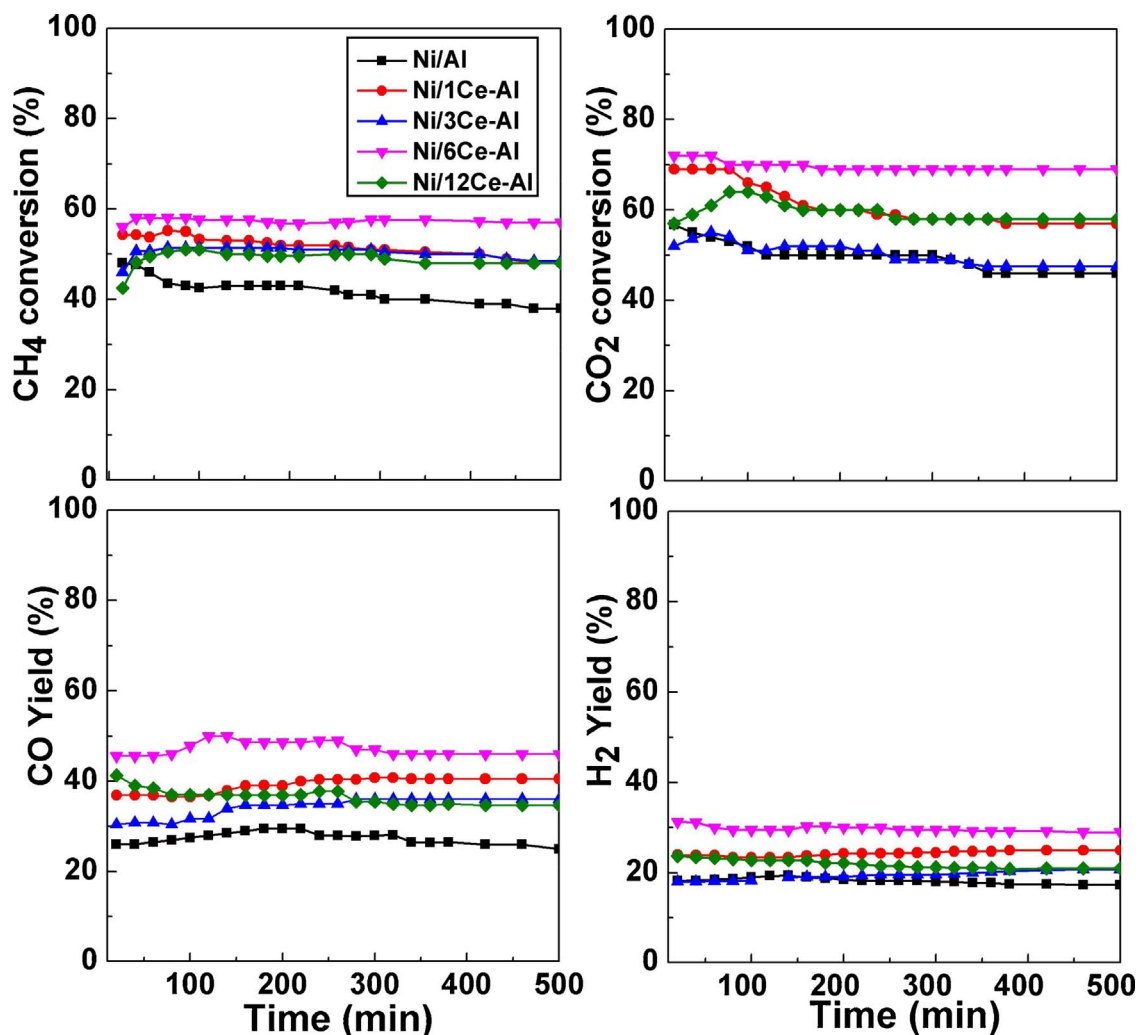


Fig. 5. Evaluation of the CH_4 and CO_2 conversions, as well as of the yields of H_2 and CO of $\text{Ni}/x\text{CeO}_2\text{-Al}_2\text{O}_3$ catalysts with time on stream in DMR at 550 °C.

interaction between the separated small nickel clusters, which leads to some broadening of the line width.

3.2. Catalyst activity test

The evaluation of CH_4 and CO_2 conversions, as well as of the yields of H_2 and CO of Ni/Al and $\text{Ni}/x\text{CeO}_2\text{-Al}_2\text{O}_3$ catalysts with time on stream in the reaction of CH_4 with CO_2 at temperature of 550 °C and ratio of $\text{CH}_4:\text{CO}_2 = 1:1$ are shown in Fig. 5. The values of CH_4 and CO_2 conversions and of H_2 and CO yields, as well as of the H_2/CO ratios for the catalysts are listed in Table 4. The data in Table 4 are taken at steady state activity. All $\text{Ni}/x\text{CeO}_2\text{-Al}_2\text{O}_3$ catalysts display CH_4 conversion values (47–57%) higher than those of non-modified with ceria alumina-supported Ni (39%) suggesting the promoting effect of ceria. Methane conversion follows the following sequence: $\text{Ni}/\text{Al} < \text{Ni}/3\text{Ce}$

Table 4

Catalytic properties of $\text{Ni}/x\text{CeO}_2\text{-Al}_2\text{O}_3$ catalysts in reforming of CH_4 with CO_2 at 550 °C reaction temperature ($\text{CH}_4/\text{CO}_2 = 1:1$; $m_{\text{cat}} = 0.05 \text{ g}$).

Sample	X_{CH_4} (%)	X_{CO_2} (%)	Y_{H_2} (%)	Y_{CO} (%)	H_2/CO
Ni/Al	39	46	17	26	0.65
Ni/1Ce-Al	50	56	25	40	0.63
Ni/3Ce-Al	50	52	20	36	0.59
Ni/6Ce-Al	57	69	29	46	0.63
Ni/12Ce-Al	47	58	21	35	0.62

$\sim \text{Ni}/1\text{Ce-Al} < \text{Ni}/12\text{Ce-Al} < \text{Ni}/6\text{Ce-Al}$. It means that the most active catalyst is $\text{Ni}/6\text{CeO}_2\text{-Al}_2\text{O}_3$. The higher H_2 and CO yields values for CeO_2 -containing Ni catalysts in relation to those of the non-modified with ceria alumina-supported Ni catalyst means that the addition of ceria improves the performance of all catalysts, but this improvement is more marked for $\text{Ni}/6\text{Ce-Al}$ catalyst.

The values of CO_2 conversions of all catalysts are higher than those of CH_4 conversions, that is usually influenced by the simultaneous occurrence of the reverse of water gas shift reaction (WGSR) ($\text{CO}_2 + \text{H}_2 \leftrightarrow \text{CO} + \text{H}_2\text{O}$), thermally favored at temperature < 600 °C, as was suggested by Bradford and Vannice [59] and others authors [60]. They suggested that the activation energy for the formation of hydrogen is always greater than that of the CO formation [59,60]. Higher CO_2 conversions are observed for all CeO_2 -loaded Ni catalysts relative to that of non-promoted with ceria sample. This reflects on the H_2/CO ratios values of the catalysts, which are lower than 1.

An induction period in dry methane reforming is observed for Ni catalysts with $\text{CeO}_2 \geq 3 \text{ wt\%}$ (Fig. 5). This should be related to the increase of the number of the active metal sites at the beginning of reaction and to change of the electron density of the active sites, which leads to a change of the adsorption of the molecules reactants. As was shown by the XPS analysis (Table 2), the previously reduction of nickel oxide species to metallic nickel is not full at 550 °C under hydrogen atmosphere. However, the NiO species continue to be reduced to metal particles by the syngas production as it is evident for the spent catalysts in Table 2. The induction period is not observed for Ni/Al catalyst,

which is characterized by a decrease of the CH_4 conversion at the beginning of reaction followed by a slowly change of methane conversion with time on stream. Probably this should be related with the agglomeration of nickel particles and/or covering by carbon species.

There is not linear change of the yields of CO and H_2 with the increase of CeO_2 loading (Table 4). Modification of $\text{Ni}/\text{Al}_2\text{O}_3$ catalyst with a small amount of ceria (1 wt%) leads to improving the H_2 yield. Maximum H_2 and CO yields are obtained for $\text{Ni}/6\text{CeO}_2\text{-Al}_2\text{O}_3$. The defined H_2/CO ratios for the reaction products mixture is below one. It is seen that the difference in the H_2/CO ratios reflects the differences in the catalytic activity and the lower reactant conversions yields a lower H_2/CO ratio. The reverse of water gas-shift reaction as a side reaction is responsible for the low H_2/CO ratios [59] listed in Table 4.

The behaviors of $\text{Ni}/x\text{CeO}_2\text{-Al}_2\text{O}_3$ catalysts with 1, 3 and 12 wt.% remain relatively stable with time on stream in the reaction of DMR at 550 °C (Fig. 5). The Ni catalyst with 6 wt% CeO_2 exhibits the highest stability. Non-promoted with ceria alumina-supported Ni catalyst exhibits a strong deactivation with time on stream the first hours of work at 550 °C.

The changes of the conversions of CH_4 and CO_2 and of the yields of CO and H_2 for $\text{Ni}/6\text{Ce-Al}$ catalyst as a function of the reaction temperatures are sown in Fig. 6. The CH_4 conversion values rich approximately 90% and those of CO_2 are near 100% at reaction temperature of 750 °C. The H_2/CO ratio value of this catalyst is increased to 1.61 at 750 °C.

It is well known that the catalyst stability depends on the particle size, as well as on the kind of deposited carbon and its location on the catalyst surface. In order to obtain information about the possible reasons of the different behaviors of catalysts at 550 °C having different surface carbon concentration according to the XPS analysis, the kind of deposited carbon was investigated by TG/TDA, TPO, Raman and HRTEM.

3.3. Characterization of carbon in spent catalysts

3.3.1. Thermogravimetric analysis

The amount and reactivity of deposited carbon on the spent catalysts with oxygen was measured by the CO_2 evolution during the temperature-programmed oxidation. The DTA and TG profiles of spent supported Ni catalysts during the TPO are shown in Fig. 7. The DTA curves of all catalysts show peaks in two temperature regions: a small one at low temperature region of 330–500 °C and a stronger asymmetric peak at higher temperature region of 500–700 °C. The asymmetric shape of CO_2 profile indicates a complex structure of the carbon species on catalysts surface. According to the literature data [61,62] the low temperature interval has been assigned to the presence of amorphous carbon. Since the oxidation temperature of large carbon fibers and nanotubes requires temperatures higher than 700–800 °C [63] the

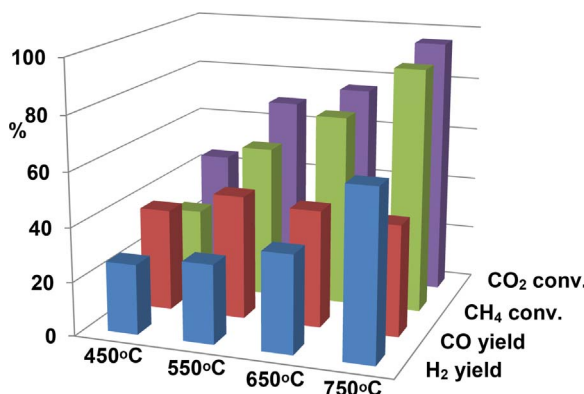


Fig. 6. The behavior of $\text{Ni}/6\text{CeO}_2\text{-Al}_2\text{O}_3$ catalyst at various reaction temperatures in DMR.

peaks at higher temperature interval should be generated from the combustion of graphitic type carbons, like small carbon filaments. From the Fig. 7 it can be concluded that the modification of alumina support with ceria affects the oxidation temperature and the amount of deposited carbon species. The addition of small amount of ceria (1 wt%) to Ni catalyst leads to a shift of the main peak to lower values (from 594° to 585 °C), as well as to a decrease of the amount of deposited carbon (from 6.6 to 2.2%, Fig. 7). The lowest oxidation temperature (579 °C), as well as the lowest weight loss (1.2%) are observed for catalyst with the highest CeO_2 content, which is in line with the lowest amount of the strong acid sites. It can be inferred that ceria plays an important role in diminishing the carbon deposition over catalysts under reaction conditions. It should be noted that the Ni catalyst with 6 wt.% CeO_2 exhibits a peak with a maximum at 612 °C, which is slightly higher than that of $\text{Ni}/\text{Al}_2\text{O}_3$, but the amount of deposited carbon is significantly lower than that of the nonpromoted with ceria sample (Fig. 7). Among the CeO_2 -containing samples the evaluated deposited carbon is slightly higher for spent $\text{Ni}/6\text{Ce-Al}$ catalyst.

Different carbon species can be deposited on the catalyst surface during the DRM reaction, whose nature strongly depends on the reaction temperature [4,5]. Thermodynamic calculations indicated that the formation of carbon species is favorable at temperatures as high as 750–800 °C [3,4]: $\text{CH}_4 \rightarrow \text{C} + \text{H}_2$ ($\Delta G = -127.66 \text{ kJ/mol}$; 827 °C). The formation of graphite (crystalline) platelet films is expected at 500–550 °C, whereas vermicular filaments or whiskers appear to be formed at 300–1000 °C [5]. Since the DRM reaction was performed at 550 °C, it is possible that some of these species are formed on the surface of the Ni-based catalysts.

It can be concluded that despite the positive effect of CeO_2 on catalyst activity, the carbon deposition would be driven by the nickel crystallite size, which influences the origin and reactivity of carbon species.

3.3.2. Raman spectra

The nature of deposited carbon on the surface of spent Ni catalysts was investigated by Raman spectroscopy, which is a powerful technique for characterization of carbon structure. The Raman spectra of spent catalysts in the range 400–1800 cm^{-1} are shown in Fig. 8. For all samples, two main bands at ca. 1351 cm^{-1} and ca. 1596 cm^{-1} are registered, which can be related to different structures of deposited carbon formed on the catalyst surface under reaction conditions. In addition, Raman spectra of $\text{Ni}/\text{Al}_2\text{O}_3$ and of the samples with 1–3 wt.% CeO_2 exhibit a small shoulder at ca. 1530 cm^{-1} , whereas that of spent catalyst with the highest CeO_2 content of 12 wt.% shows a small band at 1441 cm^{-1} . The low frequency band (called as D-band), which is more intensive than the higher frequency band (called as G-band) can be attributed to the vibration of carbon atoms with dangling bonds in disordered carbonaceous species, such as amorphous or defective filaments [64]. Whereas, the G-band is assigned to the well-ordered carbon species as the sp^2 bonded carbon atoms in a two-dimensional hexagonal lattice, such as in a graphite layer [63].

Taking in mind the relative intensities of the both main bands [64], it is interesting to note that the Ni sample with 6 wt.% CeO_2 exhibits a slightly higher ordering degree of carbon species within the CeO_2 -containing spent catalysts. The results agree well with the TG analysis, where the less ordered carbon causes a lower carbon oxidation temperature and the amount of this species is in a higher proportion for all samples, being seen in Fig. 7. It suggests that the addition of CeO_2 is effective in suppressing the growth of high ordered carbon species, like large filaments or nanotubes

3.3.3. HRTEM

The morphology of reduced and spent catalysts was analyzed by HRTEM. TEM images of some fresh reduced and spent catalysts are shown in Fig. 9. The evaluated particle size of the reduced and spent Ni catalysts are presented in Fig. 10A and 10B, respectively. As can be

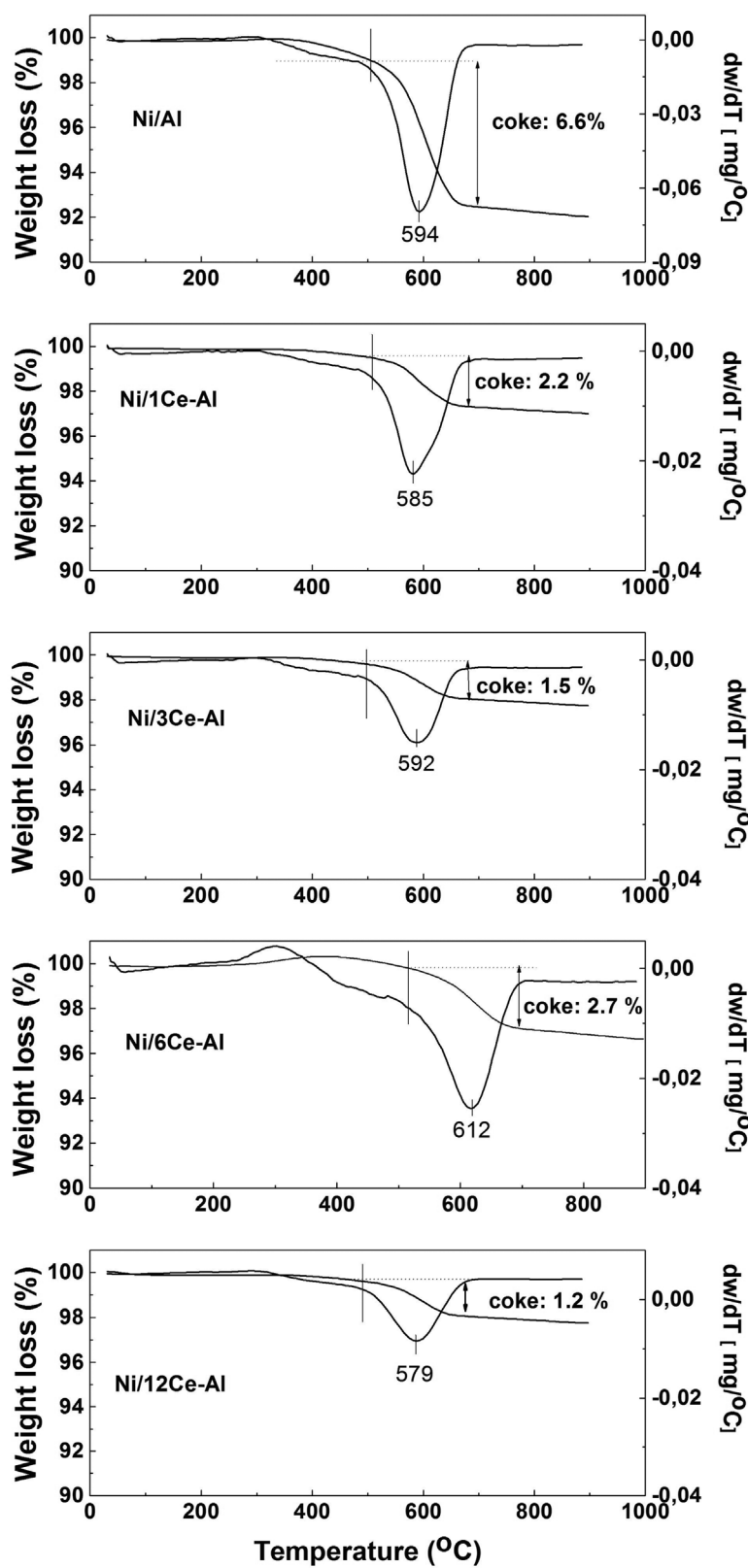


Fig. 7. Temperature programmed oxidation of spent $\text{Ni}/x\text{CeO}_2\text{-Al}_2\text{O}_3$ catalysts with different CeO_2 content.

concluded from Fig. 9 a great number of exposed Ni species are located on the surface of reduced ceria-containing samples with 6 and 12 wt.% CeO_2 . It is obvious that the average particle size of reduced CeO_2 -containing Ni samples (4.2–4.7 nm) relative to that of non-promoted alumina-supported Ni (5.6 nm) is smaller. There is some agglomeration of nickel particles for all spent catalysts in comparison to that observed

for reduced samples, which is more obviously for Ni/Al (Fig. 10). The largest average particle size of 8.5 nm and a more heterogeneous particle size distribution from 0.5 nm up to 20 nm after work is observed for non-promoted with ceria Ni catalyst. In addition, that catalyst produces some carbon filaments (Fig. 9), which is in agreement with the largest amount of deposited carbon species according to the XPS

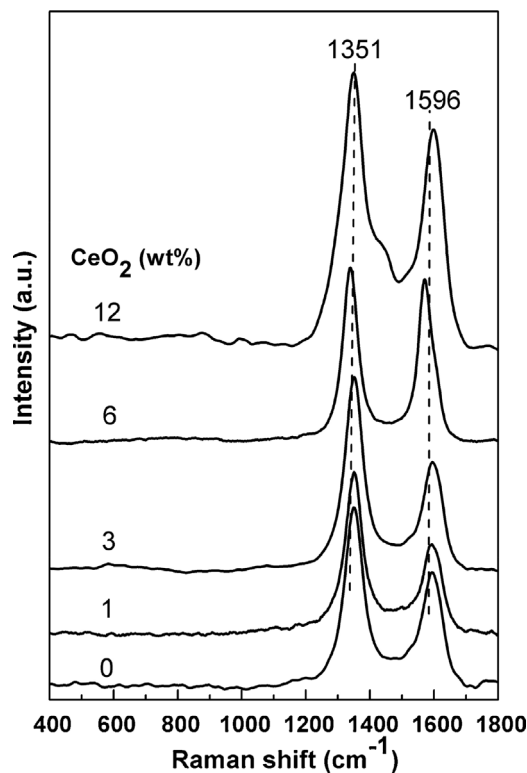


Fig. 8. Raman spectra of spent Ni/ x CeO₂-Al₂O₃ catalysts with different CeO₂ content.

and TPO data (Table 2 and Fig. 7). The spent CeO₂-containing Ni catalysts are characterized with smaller particles and more homogeneous particle size distribution as the particles with size below 7 nm dominate (Fig. 10).

4. Discussion

4.1. The effect of CeO₂ content on the characteristic of Ni catalysts

Based on the physicochemical characterization it can be concluded that the Ni-support and Ce-alumina interactions in x CeO₂-Al₂O₃-supported Ni catalysts could affect either the degree of Ni sintering or the ability of dispersed Ni to adsorb hydrogen. The results clearly show that there is a difference in the oxidation state of supported Ce and Ni species with the change of CeO₂ content and their exposure to different atmospheres.

The electronic environment of the cerium and nickel cations are changed with CeO₂ content. The cerium is stabilized in two oxidation states of Ce⁴⁺ and Ce³⁺ for supported Ni catalysts, as well as for mixed x CeO₂-Al₂O₃ oxides, being supported by the XPS and UV-vis DRS. There are different reasons that cause the low oxidation state of cerium. As was shown above, it can be proposed that part of Ce is atomically dispersed on alumina as Ce³⁺ due to the strong interaction between cerium and aluminium species, stabilizing cerium in a lower oxidation state of 3+. This is more obviously for the lower CeO₂-loaded samples (≤ 3 wt.%), which can prevent the loss of the support thermal stability. The strong interaction between the dispersed Ce and alumina results in the formation of a surface CeAlO₃ by occupation of the vacant octahedral sites on alumina surface by Ce³⁺ cations [65]. But, the TPR detected the reduction of CeAlO₃ after complete reduction of CeO₂ only, i.e. at higher reduction temperature of 890 K due to the diffusion limitation of cerium [35]. The relatively high density of the Ce³⁺ exposed on the surface of all oxidic Ni samples, as well as on the surface of the mixed x CeO₂-Al₂O₃ oxides, revealed by the change of the XPS atomic Ce³⁺/Ce⁴⁺ + Ce³⁺ ratios values, should be additionally related to some partial reduction of Ce⁴⁺ during the XPS measurements under vacuum. A progressive elimination of the surface hydroxyl groups and oxygen in the CeO₂ with fluorite structure can occur under vacuum treatment [34].

The cerium oxides are other species for both systems, as their size depends also on the CeO₂ content. The lowest CeO₂-loaded Ni sample of

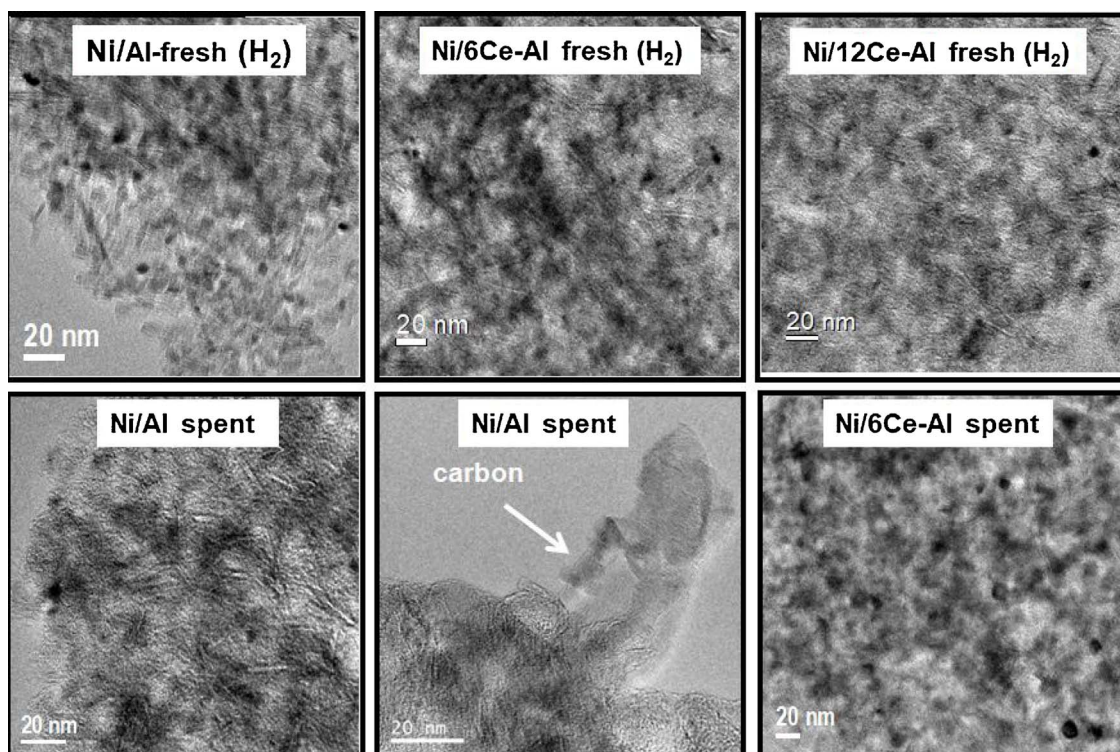
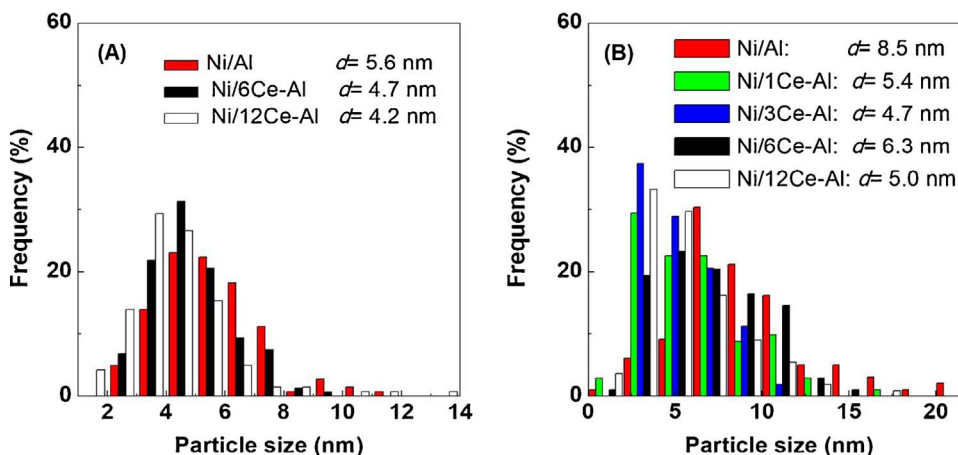


Fig. 9. TEM images of reduced and spent Ni/ x CeO₂-Al₂O₃ catalysts with different CeO₂ content.



1 wt.% CeO₂ possesses very small ceria particles, being supported by the absence of the XRD patterns of bulk CeO₂ (< 4 nm). However, the increase of CeO₂ content ≥ 3 wt.% leads to the agglomeration of CeO₂ particles from 5.5 nm to 9.3 nm for Ni/3CeO₂-Al₂O₃ and Ni/12CeO₂-Al₂O₃, respectively (Table 1).

It is important to note that the presence of the Ce³⁺/Ce⁴⁺ couple in the oxidic samples is kept for all samples under the reductive and reaction conditions. The number of the exposed cerium species for supported Ni catalysts revealed by the atomic Ce/Al ratios is decreased under hydrogen atmosphere, relative to that for fresh samples, probably due to a sintering. However, there is a recovering of the dispersion of cerium species of all spent catalysts, near to that of oxidic samples, which is more visible for the sample with 12 wt.% CeO₂ (Table 2).

XRD, UV-vis DRS, XPS, TPR and EPR data confirm that the oxidation state of Ni species in oxidic, reduced and spent catalysts depends on the CeO₂ content. For oxidic Ni samples the registered Ni²⁺ ions are in different environments: in tetrahedral configuration due to the formation of surface species with structure, like NiAl₂O₄ spinel and in octahedral configuration as NiO, being confirmed by UV-vis DRS and XPS. The formation of surface NiAl₂O₄ species is preventing with the increase of CeO₂ loading. Similar observations have been observed after adding of CeO₂ to previously reduced alumina-supported Ni catalysts [66]. For the reduced and spent catalysts the nickel oxide species are partly reduced to metallic nickel, as the amount of Ni⁰ is enhanced under reaction conditions (Table 2), but it is the lowest for the highest CeO₂-loaded sample.

It is well known the effect of CeO₂ on the increase of dispersion of various supported metals. For the fresh CeO₂-containing Ni samples the dispersion of nickel species, revealed by the change of the atomic Ni/Al + Ce ratios (Table 2), is higher compared to that of alumina-supported sample. Among all catalysts, the Ni/CeO₂-Al₂O₃ catalyst with CO₂ loading of 6 wt.% exhibits the highest Ni dispersion after reduction and reaction, but it is slightly decreased for spent catalyst. As was shown above, the high dispersion causes a specific interaction between the nickel and ceria species. The well dispersed metallic Ni particles close to the ceria activate the hydrogen dissociation and by hydrogen spillover favors the reduction of ceria surface. Thus, the temperature region related to the surface reduction of ceria is shifted to lower temperatures, supported by the TPR data. In the same time, the great number of the formed O²⁻ species possessing a high electron density could facilitate the increase of the electron density of Ni by charge transfer [6], as it is detected for Ni catalyst with 6 wt.%. (Table 2). This additionally leads to the increase of hydrogen consumption for higher CeO₂-loaded Ni catalysts (6 and 12 wt.%), being seen in Fig. 3B.

4.2. Catalysts behaviors

Comparing the activities related to the conversions of CH₄ and CO₂

at reaction temperature of 550 °C (Table 4, Fig. 5) it can be summarized that the difference in the catalysts behaviors should be connected with the difference in the number of the exposed active sites. It is obviously, that several variables affect the catalyst activity depending on the CeO₂ content. The results clearly show that the initial activity of ceria-loaded Ni catalysts is greatly influenced by the oxidation state, dispersion and decoration of the nickel sites. The increase of the electron density of Ni sites under reaction conditions should be influenced by two ways: (i) the additional reduction of nickel oxide species by hydrogen atoms from the produced H₂ and (ii) the close contact between ceria and nickel species. However, the non-modified with ceria alumina-supported Ni catalyst exhibits a decrease of CH₄ conversion the first hours of work, followed by a slowly change in activity. The behavior of Ni/Al catalyst can be associated with the presence of agglomerated nickel particles causing the formation of more carbon species (Figs. 7–10).

The difference in the catalytic behaviors of the samples can be strongly affected by the nature of the carrier, suggesting that the activity and the rate of deactivation is likely to be related to the different extent of electronic interaction between supported metal and support, influencing the bonding and reactivity of the chemisorbed species. The presence of Ni²⁺/Ni⁰ and Ce⁴⁺/Ce³⁺ couples means that different species can take participation in the activation of CH₄ and CO₂ molecules. According to Bazin et al. [67] an increase of the local electron density is expected with increasing the metal dispersion, as it is well visible for catalyst with 6 wt.% CeO₂. This catalyst exhibits a great number of active sites accessible to the reactants molecules compared to that observed for other CeO₂-containing catalysts.

The significant difference in the behaviors of the both catalysts, Ni/Al and Ni/6Ce-Al, should be mainly connect with the difference in their dispersions. Since the CH₄ dissociation and coke formation take place on the surface of metallic Ni particles [68] the great difference in CH₄ conversions and stabilities of these catalysts is associated with the different coke behavior caused by the different degree of nickel dispersion on catalyst surface. The change of the average particle size for all spent catalysts is in the following order: Ni/3Ce-Al(4.7 nm) < Ni/12Ce-Al (5.0 nm) < Ni/1Ce-Al(5.4 nm) < Ni/6Ce-Al(6.3 nm) < Ni/Al (8.5 nm) (Fig. 10). It means that non-promoted Ni catalyst exhibits the highest average particle size and a heterogeneous particle size distribution from 0.5 nm to about 20 nm. The change of the average particle size for spent CeO₂-containing catalysts is negligible relative to that of the reduced ones (Fig. 10) suggesting very good anti-sintering properties. It means that supported cerium and nickel species in ceria-loaded Ni catalysts are well located on the walls of mesopores of γ -Al₂O₃, enhancing their dispersion and coking resistance.

Usually, a large amount of CeO₂ promoter leads to a decrease of catalytic activity due to the partly coverage of the active sites by ceria. The catalyst with the highest amount of CeO₂ (12 wt.%) gives possibly less reducible nickel species and Ni appears to be continuously reduced

under reaction conditions, similar to other ones. Thermal and chemical effects during the high temperature reduction can induce a migration of partially reduced ceria species (CeO_x) to the metal surface. By this way, the nickel particles are partially covered by thin layer of reduced support causing a blockage of the active catalytic centers to the reactants molecules. Similar effect has been observed in Refs. [30,32].

On the other hand, it has been suggested [69,70] that the decoration of metallic particles by the support species is responsible for decreasing the rate of the formation and the growth of carbon filaments during the reaction. It is well known [52] that coke during methane reforming reactions can be formed by the conversion of accumulated carbon atoms to less reactive carbon species, which may encapsulate the surface of Ni^0 or to dissolve in the nickel crystallites. The dissolved carbon diffuses through the nickel to nucleate at metal-support interface forming carbon filaments, on the top of which the active metal particle can be situated. This phenomenon is observed for non-promoted with ceria Ni/Al catalyst, being seen in Fig. 9.

It is important to note that the intimate contact between nickel and ceria species as a result of the high nickel dispersion could lead to a negative effect on the catalysts performances due to the difficulty of Ni^{2+} reducibility to Ni^0 and of the CH_4 adsorption. Nevertheless, the intimate contact between the cerium oxide species and Ni can facilitate the interaction of the metal surface with methane. According to kinetic studies [70] it has been found that Ni and O atoms work in a cooperative way to dissociate the CH_4 molecule. Adsorption sites with adjacent Ni and O atoms exist in the CeO_2 -promoted Ni catalyst system. In addition, the presence of the $\text{Ni}^{2+}/\text{Ni}^0$ couple offers different kinds of nickel species. Since the chemisorbed CH_4 molecules are more stable on Ni^0 than on Ni^{2+} sites [70], this increases the probability for reaction at the $\text{Ni}^0\text{-CeO}_{2-x}$ interface. Due to the high density of O^{2-} species at the interface Ni-cerium oxide species, being confirmed by the TPR, the oxygen atoms can move to react with C species from the fast CH_4 dissociation and to form CO. On the other hand, the presence of a great number of accessible basic O^{2-} species could promote the CO_2 dissociation, similar to that observed for Ni catalyst supported on basic La_2O_3 carrier [22].

It can be assumed that CeO_2 favors the metallic dispersion and inhibits the formation of large metallic assemblies and improves the resistance to carbon formation. In spite of the larger amount of surface carbon deposits registered for the most active Ni/6Ce-Al catalyst and taking in mind the higher dispersion revealed by the highest Ni/Ce + Al ratio value for this catalyst (Table 2), it can suppose that the carbon species is not located on the active sites of this catalyst, i.e. they are in the periphery of nickel. The high activity of Ni/6Ce-Al is connected with the great number of accessible active Ni sites exposed at the catalyst surface. It means that more active sites can participate in the activation and dissociation of methane and the activity and stability are significantly high.

5. Conclusions

The synthesized mixed $\text{CeO}_2\text{-Al}_2\text{O}_3$ oxides with different CeO_2 content (1, 3, 6 and 12 wt.%) are revealed as suitable carriers for supported Ni catalysts. The results show that the nature of nickel-support interaction in $\text{Ni/Al}_2\text{O}_3$ and $\text{Ni/xCeO}_2\text{-Al}_2\text{O}_3$ catalysts systems causes different accessibility and reducibility of both, the nickel and cerium species. Increasing the CeO_2 loading leads to agglomeration of CeO_2 phase with fluorite structure. The influence of Ni addition to the mixed oxides supports was negligible on the change of ceria particle size. The XPS analysis suggests that the intimate contact between nickel and cerium species depends on the CeO_2 content. CeO_2 -containing catalysts exhibit high coke resistance due to the presence of small nanoparticles with average particles size of 4.7–6.3 nm. Two kinds of deposited carbon on the surface of spent catalysts are registered: more ordered and less ordered carbon. The heterogeneous nickel particle size distribution from 0.5 nm to 20 nm, established for non-promoted with

ceria alumina-supported Ni catalyst, causes the formation of nanofibers and catalyst deactivation. The most active catalyst in dry reforming of CH_4 is Ni/6Ce-Al. The CeO_2 content of 6 wt.% is optimal to ensure a more intimate contact between the nickel and cerium oxide species leading to a change in the electronic properties of Ni and Ce atoms and to the increase of accessibility of the active sites for that catalyst.

Acknowledgments

The authors are acknowledged to project FNI E02/16/2014 for financial support.

References

- I. Luisetto, S. Tuti, C. Battocchio, S. Lo Mastro, A. Sodo, *Appl. Catal. A: Gen.* 500 (2015) 12–22.
- D.L. Trimm, *Catal. Rev. Sci. Eng.* 16 (1977) 155–169.
- S. Arora, R. Prasad, *RSC Adv.* 6 (2016) 108668–108688.
- X.E. Verykios, *Int. J. Hydrogen Energy* 28 (2003) 1045–1063.
- J.R. Rostrup-Nielsen, *Stud. Surf. Sci. Catal.* 36 (1998) 73–78.
- S. Kawi, Y. Kathiraser, J. Ni, U. Oemar, Z. Li, E.T. Saw, *ChemSusChem* 8 (2015) 3556–3575.
- D. Parkhore, J. Spivey, *Chem. Soc. Rev.* 43 (2014) 7813–7837.
- S. Li, J. Gong, *Chem. Soc. Rev.* 33 (2014) 7245–7256.
- K. Takehira, *J. Natural Gas Chem.* 18 (2009) 237–259.
- X. Li, H. Tian, L. Zeng, Z.-J. Zhao, J. Gong, *Appl. Catal. Environ.* 202 (2017) 683–694.
- Ya-Li Du, Xu Wu, Qiang Cheng, Yan-Li Huang, Wei Huang, *Catalysts* 7 (2017) 70–81.
- G. Wu, C. Zhang, S. Li, Z. Huang, S. Yan, S. Wang, X. Ma, J. Gong, *Energy. Environ. Sci.* 5 (2012) 8942–8949.
- S. Damyanova, B. Pawelec, K. Arishtirova, J.L.G. Fierro, C. Sener, T. Dogu, *Appl. Catal. B: Environ.* 92 (2009) 250–261.
- D. Li, K. Nishida, Y. Zhan, T. Shishido, Y. Oumi, T. Sano, K. Takehira, *Appl. Catal. A: Gen.* 310 (2006) 97–104.
- S. Damyanova, B. Pawelec, K. Arishtirova, J.L.G. Fierro, *Int. J. Hydrogen Energy* 37 (2012) 15966–15975.
- E.C. Faria, R.C.R. Neto, R.C. Colman, F.B. Noronha, *Catal. Today* 228 (2014) 138–144.
- N.D. Charisiou, G. Siakavelas, K.N. Papageridis, A. Baklavariidis, L. Tzounis, D.G. Avraam, M.A. Goula, *J. Nat. Gas Sci. Eng.* 31 (2016) 164–184.
- H. Ay, D. Uner, *Appl. Catal. B: Environ.* 179 (2015) 128–138.
- S.A. Theofanidis, V.V. Galvita, H. Poelman, G.B. Marin, *ACS Catal.* 5 (5) (2015) 30288–33039.
- A. Wolfbeisser, O. Sophiphun, J. Bernardi, J. Wittayakun, K. Föttinger, G. Rupprechter, *Catal. Today* 277 (2016) 234–245.
- S. Li, C. Zhang, G. Wu, J. Gong, *ChemComm R. Soc. Chem* 39 (2013) 4035–4426.
- Z. Zhang, X.E. Verykios, *Catal. Lett.* 38 (1996) 175–179.
- A. Slagtern, Y. Schuurman, C. Leclercq, X. Verykios, C. Mirodatos, *J. Catal.* 172 (1997) 118–126.
- A. Trovarelli, *Catal. Rev.* 38 (1996) 440–519.
- P. Kumar, Y. Sun, R.O. Idem, *Energy Fules* 22 (2008) 3575–3582.
- I. Luisetto, S. Tuti, C. Battocchio, S. Mastro, A. Sodo, *Appl. Catal. A: Gen.* 235 (2015) 302–310.
- J. Chen, R. Wang, J. Zhang, F. He, S. Han, *J. Mol. Catal. A: Chem.* 235 (2005) 302–310.
- A. Kambolis, H. Matralis, A. Trovarelli, Ch. Papadopoulou, *Appl. Catal. A* 377 (2010) 16–26.
- S.S. Kim, S.M. Lee, J.M. Won, H.J. Yang, S.C. Hong, *Chem. Eng. J.* 280 (2015) 433–440.
- S. Damyanova, J.M.C. Bueno, *Appl. Catal. A: Gen.* 253 (2003) 135–150.
- S. Damyanova, B. Pawelec, K. Arishtirova, M.V. Martinez Huerta, J.L.G. Fierro, *Appl. Catal. A: Gen.* 337 (2008) 86–96.
- S. Damyanova, B. Pawelec, K. Arishtirova, M.V. Martinez Huerta, J.L.G. Fierro, *Appl. Catal. B: Environ.* 89 (2009) 149–159.
- G. Leofanti, M. Padovan, G. Tozzola, B. Venturelli, *Catal. Today* 41 (1998) 207–219.
- S. Damyanova, A. Perez, M. Schmal, J.M.C. Bueno, *Appl. Catal. A* 234 (2002) 271–282.
- A.P. Ferreira, D. Zanchet, J.C.S. Araujo, J.W.C. Liberatori, E.F. Souza-Aguiar, F.B. Noronha, J.M.C. Bueno, *J. Catal.* 263 (2009) 335–344.
- D.K. Kim, K. Stöwe, F. Müller, W.F. Maier, J. Catal. 247 (2007) 101–111.
- C. Yu, J. Hu, W. Zhou, Q. Fan, *J. Energy Chem.* 23 (2014) 235–243.
- A. Kambolis, H. Matralis, A. Trovarelli, Ch. Papadopoulou, *Appl. Catal. A: Gen.* 377 (2010) 16–26.
- A. Bensalem, F. Bozon-Verduraz, M. Delamar, G. Bugli, *Appl. Catal. A: Gen.* 121 (1995) 81–93.
- R. Li, S. Yabe, M. Yamashita, S. Momose, S. Yoshida, S. Yin, T. Sato, *Mater. Chem. Phys.* 75 (2002) 39–44.
- A. Tisoaga, D. Visinescu, B. Jurca, A. Ianculescu, O. Carp, *J. Nanopart. Res.* 13 (2011) 6397–6408.
- C. Jimenez-Gonzalez, Z. Boukha, B. de Rivas, J.J. Delgado, M.A. Cauqui,

J.R. Gonzalez-Velasco, J.I. Gutierrez-Ortiz, *Appl. Catal. A: Gen.* 466 (2013) 9–20.

[43] J. Jun, M. Dhayal, H. J-Shin, Y.H. Han, N. Getoff, *Appl. Surf. Sci.* 254 (2008) 4557–4564.

[44] B.A. Riquetto, S. Damyanova, G. Goulev, C.M. Marques, L. Petrov, J.M.C. Bueno, *J. Phys. Chem. B* 108 (2004) 5349.

[45] X. Cai, X. Dong, W. Lin, *J. Nat. Gas. Chem.* 17 (2008) 98–102.

[46] H.C. Yao, Y.F. Yu Yao, *J. Catal.* 86 (1984) 254–2265.

[47] G. Jacobs, U.M. Graham, E. Chenu, P.M. Patterson, A. Dozier, B.A. Davis, *J. Catal.* 229 (2005) 499–512.

[48] F. Giordano, A. Trovarelli, C. de Leitenburg, M. Giona, *J. Catal.* 193 (2000) 273–282.

[49] A. Piras, S. Colussi, A. Trovarelli, V. Sergio, J. Llorca, R. Psaro, L. Sordelli, *J. Phys. Chem. B* 109 (2005) 11110–11118.

[50] J.M. Rynkowski, T. Paryjczak, M. Lenik, *Appl. Catal. A: Gen.* 106 (1993) 73–82.

[51] H. Özdemir, M.A.F. Öksüzömer, M.A. Gürkaynak, *Int. J. Hydrogen Energy* 35 (2010) 12147–12160.

[52] B.S. Liu, C.T. Au, *Appl. Catal. A: Gen.* 244 (2003) 181–195.

[53] Y. Wang, A. Zhu, Y. Zhang Y, C.T., Au, X. Yang, C. Shi C. *Appl. Catal. B: Environ.* 81, 2008, 141–149.

[54] A. Irondo, V.L. Barrio, J.F. Cambra, P.L. Arias, M.B. Guemez, M.C. Sanchez-Samchez, R.M. Navarro, J.L.G. Fierro, *Int. J. Hydrogen Energy* 35 (2010) 11622–11633.

[55] S. Damyanova, A.A. Spojakina, D.M. Shopov, *Appl. Catal.* 48 (1989) 177–186.

[56] L. Appel, A. Frydman, C. Perez, J. Eon, D. Castner, Ch. Campabell, M. Schmal, *Phys. Stat. Sol. (b)* 192 (1995) 49–477.

[57] C. Oliva, G. Termignone, F.P. Vatti, L. Fornia, V. Vishniakov, *J. Mater. Sci.* 31 (1996) 6333–6338.

[58] G. Wrobel, C. Lamoni, A. Bennani, A. D'Huysser, A. Aboukais, *J. Chem. Soc. Faraday Trans.* 92 (11) (1996) 2001–2009.

[59] M.C.J. Bradford, M.A. Vannice, *Appl. Catal. A: Gen.* 142 (1996) 73–96.

[60] I. Luisetto, S. Tuti, C. Battocchio, S. Lo Mastro, A. Sodo, *Appl. Catal. A: Gen.* 500 (2015) 12–22.

[61] A. Djajida, S. Libs, A. Kienneman, A. Barama, *Catal. Today* 13 (006) (2017) 194–200.

[62] P. Osorio-Vargas, N.A. Flores-González, R.M. Navarro, J.L.G. Fierro, C.H. Campos, P. Reyes, *Catal. Today* 259 (2015) 27–38.

[63] P. Wang E. Tanabe, K. Ito, J. Jia, H. Morioka, T. Shishido, *Appl. Catal. A: Gen.* 231 (2002) 35–44.

[64] F. Tuinstra, J.L. Koenig, *J. Chem. Phys.* 53 (1970) 1126–1113.

[65] J.Z. Shyu, K. Otto, *J. Catal.* 115 (1989) 16–23.

[66] N. Laostripojana, W. Suthisripok, S. Assabumrungrat, *Cem. Eng. J.* 1 (112) (2015) 13–22.

[67] D. Bazin, D. Sayers, J.J. Rehr, C. Matteri, *J. Phys. Chem. B* 101 (1997) 5332–5336.

[68] Z. Wang, X.M. Cao, J. Zhu, P. Hu, *J. Catal.* 311 (2014) 469–480.

[69] A.N. Fatsikostas, D. Kondarides, X.E. Verykios, *Catal. Today* 75 (2002) 145–155.

[70] Z. Liu, D. Grinter, P.G. Lustemberg, T.D. Nguyen-Phan, Y. Zhou, S. Luo, I. Waluyo, E.J. Crumlin, D.J. Stacchiola, J. Zhou, J. Carrasco, H.F. Busnengo, M.V.C. Pirovano, S.D. Senanayake, J. Rodriguez, *Angew. Chem. Int. Ed.* 55 (2016) 7455–7459.